Journal of Computational Physics 228 (2009) 2119–2131

Contents lists available at ScienceDirect

Journal of Computational Physics

journal homepage: www.elsevier.com/locate/jcp

A central conservative scheme for general rectangular grids

R. Kissmann [a,*], J. Pomoell [b], W. Kley [a]

[a] Institut für Astronomie and Astrophysik, Universität Tübingen, Auf der Morgenstelle 10, 72076 Tübingen, Germany
[b] Department of Physics, Gustaf Hällströmin katu 2a, 00014 University of Helsinki, Finland

ARTICLE INFO

Article history:
Received 21 February 2008
Received in revised form 13 October 2008
Accepted 25 November 2008
Available online 9 December 2008

Keywords:
Numerics: central schemes
Hyperbolic conservation laws
Compressible flows
General rectangular grids

ABSTRACT

We present an extension of the genuinely multi-dimensional semi-discrete central scheme developed in [A. Kurganov, S. Noelle, G. Petrova, Semidiscrete central-upwind schemes for hyperbolic conservation laws and Hamilton–Jacobi equations, SIAM J. Sci. Comput. 23 (3) (2001) 707–740.] to arbitrary orthogonal grids. The presented algorithm is constructed to yield the geometric scaling factors in a self-consistent way.

Additionally, the order of the scheme is not fixed during the derivation of the basic algorithm. Based on the resulting general scheme it is possible to construct methods of any desired order, just by considering the corresponding reconstruction polynomial. We demonstrate how a second order scheme in plane polar coordinates and cylindrical coordinates can be derived from our general formulation. Finally, we demonstrate the correctness of this second order scheme through application to several numerical experiments.

1. Introduction

Numerical methods for the solution of systems of hyperbolic conservation equations of the form:

$$\frac{\partial u}{\partial t} + \nabla \cdot \mathsf{F}(u) = 0 \tag{1}$$

are very important for many areas of physics. Here the spatial integral of u corresponds to a conserved quantity and $\mathsf{F}(u)$ is the corresponding nonlinear advection flux. The quantity u can be either a scalar (e.g., the density in the hydrodynamic continuity equation) or a vector quantity (momentum in the corresponding evolution equation), which in general depends on all three spatial coordinates. Below we will investigate the case where – due to symmetries of the corresponding problem – u only depends on two rectangular coordinates.

To solve this system of equations many numerical methods have been developed. As will be discussed later, it is necessary for these numerical methods to conserve the quantity corresponding to u in order to correctly capture discontinuities appearing in the solution (see, e.g., [20]). Traditionally, most of these numerical methods have been derived for Cartesian coordinates. For many applications, however, the geometry of the problem demands for other sets of coordinates. For example numerical investigations of stellar structure, geophysical models, simulations of accretion disc flows and analyses of positive columns can most efficiently be performed by making use of spherical or cylindrical coordinates.

To derive a scheme for curvilinear orthogonal coordinates we state the explicit form of Eq. (1) for a general rectangular grid. For two spatial dimensions (with x and y denoting arbitrary non-Cartesian coordinates) this is:

$$\frac{\partial}{\partial t}u + \frac{1}{h_1 h_2}\left(\frac{\partial}{\partial x}(h_2 f_1(u)) + \frac{\partial}{\partial y}(h_1 f_2(u))\right) = S(x,y) \tag{2}$$

* Corresponding author. Tel.: +49 70712977683.
E-mail address: ralf.kissmann@uni-tuebingen.de (R. Kissmann).

0021-9991/$ - see front matter © 2008 Elsevier Inc. All rights reserved.
doi:10.1016/j.jcp.2008.11.030

possibly including some geometrical source terms $S(x,y)$ on the right. These source terms can arise, when u is a vectorial quantity. In this case the divergence of the tensorial flux function $\mathsf{F}(u)$ can yield (inertial) terms, which do not contain any derivatives of u, when evaluated in non-Cartesian curvilinear coordinates. Since these source terms can be included more or less trivially into the algorithm, we will concentrate only on the hyperbolic part of the base scheme. Additionally, h_1 and h_2 are the geometrical scale factors, which depend on the coordinates under consideration, and f_1 and f_2 are the two individual components of the flux function $\mathsf{F}(u)$.

In the present paper we will focus on finite-volume central schemes due to their generality, which make them basically independent of the eigenstructure of the system of equations to be solved. This has to be seen in contrast to upwind schemes (like, e.g., the Godunov scheme – see [10]), where a Riemann solver and a characteristic decomposition is applied. Therefore, central schemes can be implemented in a universal way and can then be applied without change to different systems of equations. The basis of these central schemes is the well-known Lax–Friedrichs method [9]. Over the years this scheme has been improved by the development of higher order methods (see, e.g., [26,25,6] or [21]). Corresponding multi-dimensional versions of these schemes were developed, e.g., in Refs. [1,3,2,5,17,23] and [22]. These, again were implemented for unstructured grids, e.g., in Refs. [4,18].

One remaining problem with the early central schemes is that they cannot be used with an arbitrarily small time-step. This is due to an accumulation of numerical dissipation (see, e.g., [16] for a discussion), leading to the problem that these schemes are not suitable for steady state simulations. The solution to this problem was an integration over Riemann fans of variable width, which is determined by the maximum local signal propagation speed. Thereby, a non-staggered fully discrete scheme could be derived, which was then transformed into a semi-discrete form (meaning a scheme, which was developed for the limit $\Delta t \to 0$). As is extensively discussed in [19], this form of the scheme has the advantage of a reduced dissipation as compared to the fully discrete schemes. This is due to the fact that the fully discrete schemes obey a restricted CFL stability condition (see [8] for a general discussion of the time-step limit), $\Delta t \sim (\Delta x)^2$, which leads to an accumulation of numerical errors due to the high number of time-steps. In contrast, the time-step of a semi-discrete scheme is determined by the convective CFL limit, thus, allowing for much larger time-steps. An extension of this scheme to third order was presented in [15], and the extension to multi-dimensions is discussed in Ref. [16].

All these schemes have in common that the change of the cell averaged conserved quantities is given as a function of their point values on the cell boundaries. In order to compute these point values a reconstruction from the cell averages is required, the order of which basically determines the order of the resulting scheme. This reconstruction has to be chosen carefully to suppress spurious oscillations at steep gradients in the resulting flow. Here, different strategies may be applied, for example the application of limiters such as minmod.

In this paper we will not discuss the fine aspects of the reconstruction – this has already been done by several authors (see, e.g., [11,12,34,27,26,28,24,14,22] or [15]). We rather intend to develop the extension of the multi-dimensional semi-discrete schemes to general orthogonal geometries. The resulting algorithm has a very general form: It is still possible to choose the desired reconstruction, thus, leaving the choice of the order of the scheme to the user. In order to minimise the numerical dissipation we stick to the idea of an integration over locally varying Riemann fans. The paper is organised as follows: in Section 2 we start by deriving the scheme in a way that is independent of the resulting geometry and the reconstruction. To enhance readability we will, however, derive the scheme only for two spatial dimensions. This derivation is easily extensible to higher dimensions (the results for the three-dimensional scheme are given in Appendix A). In Section 3 we will consider the derivation of the special cases of plane polar and cylindrical coordinates from the general scheme in detail, which is followed by a discussion of numerical experiments in Section 4. We end with the conclusion of this paper.

2. General form for the semi-discrete scheme

Our starting point for the derivation of the general two-dimensional scheme for arbitrary orthogonal coordinates is Eq. (2). Here we choose $t^n = n\Delta t$ for the temporal grid and $x_i = h_1(x,y)i\Delta x$, $y_j = h_2(x,y)j\Delta y$ for the spatial grid, where $h_1(x,y)$ and $h_2(x,y)$ are the scale factors for the corresponding orthogonal coordinate system, which in general are given by the relation $h_i = \sqrt{g_{ii}}$. Here g_{ii} are the diagonal elements of the corresponding metric tensor. Thus, the individual cells $C_{i,j}$ have the extent $x_i \pm h_1(x_i,y_j)\frac{\Delta x}{2}$ and $y_j \pm h_2(x_i,y_j)\frac{\Delta y}{2}$ leading to the cellular area:

$$|C_{i,j}| = \int_{x_{i-\frac{1}{2}}}^{x_{i+\frac{1}{2}}} \int_{y_{j-\frac{1}{2}}}^{y_{j+\frac{1}{2}}} h_1(\xi,\eta)h_2(\xi,\eta)d\xi\, d\eta \tag{3}$$

For every time-step we obtain a piecewise polynomial reconstruction of the desired order from the cell averages obtained at the end of the previous time-step $\bar{u}^n_{i,j} := \bar{u}(x_i,y_j,t^n)$. This reconstruction is given by:

$$\tilde{u}^n(x,y) := \sum_{i,j} p^n_{i,j}(x,y)\chi_{i,j} \tag{4}$$

where $\chi_{i,j}$ is the characteristic function of the same cell and $p_{i,j}(x,y)$ is the reconstruction polynomial for the same cell. The reconstruction polynomial has to fulfil:

$$\bar{u}^n_{ij} = \frac{1}{|C_{ij}|}\int_{x_{i-\frac{1}{2}}}^{x_{i+\frac{1}{2}}}\int_{y_{j-\frac{1}{2}}}^{y_{j+\frac{1}{2}}} p^n_{ij}(\xi,\eta)h_1(\xi,\eta)h_2(\xi,\eta)d\xi\,d\eta \tag{5}$$

This piecewise polynomial interpolant may be discontinuous only at the cell boundaries $x = x_{i\pm\frac{1}{2}}$ or $y = y_{j\pm\frac{1}{2}}$. In a short time Δt these discontinuities can propagate a small distance, which depends on the local signal propagation velocity. The regions, in which such discontinuities can occur are highlighted in Fig. 1, where a cell for a non-Cartesian grid is visualised. Their extent is determined by the local maximum of the signal propagation velocity. Here the dark grey areas may contain discontinuities in both of the grid directions, whereas the light grey areas may only contain such in one of the grid directions. In this work we will be using the following estimate for these sub-regions of the cell $C_{i,j}$:

$$\begin{aligned} D_{i,j+\frac{1}{2}} := {} & [h_1(x_{i-\frac{1}{2}},y_{j+\frac{1}{2}})x_{i-\frac{1}{2}} + a^+_{i-\frac{1}{2}j+\frac{1}{2}}\Delta t,\quad h_1(x_{i+\frac{1}{2}},y_{j+\frac{1}{2}})x_{i+\frac{1}{2}} - a^-_{i+\frac{1}{2}j+\frac{1}{2}}\Delta t] \\ & \times [h_2(x_i,y_{j+\frac{1}{2}})y_{j+\frac{1}{2}} - b^-_{ij+\frac{1}{2}}\Delta t,\quad h_2(x_i,y_{j+\frac{1}{2}})y_{j+\frac{1}{2}} + b^+_{ij+\frac{1}{2}}\Delta t] \end{aligned} \tag{6}$$

$$\begin{aligned} D_{i+\frac{1}{2}j} := {} & [h_1(x_{i+\frac{1}{2}},y_j)x_{i+\frac{1}{2}} - a^-_{i+\frac{1}{2}j}\Delta t,\quad h_1(x_{i+\frac{1}{2}},y_j)x_{i+\frac{1}{2}} + a^+_{i+\frac{1}{2}j}\Delta t] \\ & \times [h_2(x_{i+\frac{1}{2}},y_{j-\frac{1}{2}})y_{j-\frac{1}{2}} + b^+_{i+\frac{1}{2}j-\frac{1}{2}}\Delta t,\quad h_2(x_{i+\frac{1}{2}},y_{j+\frac{1}{2}})y_{j+\frac{1}{2}} - b^-_{i+\frac{1}{2}j+\frac{1}{2}}\Delta t] \end{aligned} \tag{7}$$

$$\begin{aligned} D_{i+\frac{1}{2}j+\frac{1}{2}} := {} & [h_1(x_{i+\frac{1}{2}},y_{j+\frac{1}{2}})x_{i+\frac{1}{2}} - a^-_{i+\frac{1}{2}j+\frac{1}{2}}\Delta t,\quad h_1(x_{i+\frac{1}{2}},y_{j+\frac{1}{2}})x_{i+\frac{1}{2}} + a^+_{i+\frac{1}{2}j+\frac{1}{2}}\Delta t] \\ & \times [h_2(x_{i+\frac{1}{2}},y_{j+\frac{1}{2}})y_{j+\frac{1}{2}} - b^-_{i+\frac{1}{2}j+\frac{1}{2}}\Delta t,\quad h_2(x_{i+\frac{1}{2}},y_{j+\frac{1}{2}})y_{j+\frac{1}{2}} + b^+_{i+\frac{1}{2}j+\frac{1}{2}}\Delta t] \end{aligned} \tag{8}$$

Here $a^\pm$ and $b^\pm$ are the maximum physical propagation velocities of any signal to the right (+) and left (−) in the x- and y-directions, respectively. These can also be specified by a mathematical expression:

$$a^+_{i+\frac{1}{2}j} = \max\left\{\lambda_{max}\left(\frac{\partial f_1}{\partial u}(u^+_{i+\frac{1}{2}j})\right), \lambda_{max}\left(\frac{\partial f_1}{\partial u}(u^-_{i+\frac{1}{2}j})\right), 0\right\} \tag{9}$$

$$a^-_{i+\frac{1}{2}j} = -\min\left\{\lambda_{min}\left(\frac{\partial f_1}{\partial u}(u^+_{i+\frac{1}{2}j})\right), \lambda_{min}\left(\frac{\partial f_1}{\partial u}(u^-_{i+\frac{1}{2}j})\right), 0\right\} \tag{10}$$

where λ_{max} and λ_{min} are the largest and smallest eigenvalues of the Jacobian $\partial f_1/\partial u$, respectively. The corresponding propagation velocities $b^\pm_{i+\frac{1}{2}j}$ in the y-direction are defined in a similar way. Here $u^\pm_{i+\frac{1}{2}j}$ are the left-/right-handed pointvalues at centre of the cell faces, which can be obtained from the polynomial reconstruction by:

$$u^+_{i+\frac{1}{2}j} := p_{i+1\,j}(x_{i+\frac{1}{2}},y_j) \quad \text{and} \quad u^-_{i+\frac{1}{2}j} := p_{ij}(x_{i+\frac{1}{2}},y_j) \tag{11}$$

With the above definitions for the possibly non-smooth regions the smooth central region is given as:

$$D_{ij} = [h_1(x_{i-\frac{1}{2}},y_j)x_{i-\frac{1}{2}}, h_1(x_{i+\frac{1}{2}},y_j)x_{i+\frac{1}{2}}] \times [h_2(x_i,y_{j-\frac{1}{2}})y_{i-\frac{1}{2}}, h_2(x_i,y_{j+\frac{1}{2}})y_{j+\frac{1}{2}}] \setminus \bigcup_{\pm}[D_{ij\pm\frac{1}{2}} \cup D_{i\pm\frac{1}{2}j} \cup D_{i\pm\frac{1}{2}j\pm\frac{1}{2}}] \tag{12}$$

The desired numerical scheme can now be obtained in a three-step procedure. First Eq. (2) is integrated over the individual sub-areas of the cell introduced above and over one time-step $[t^n, t^{n+1}]$. This yields local cell averages for the next time-step

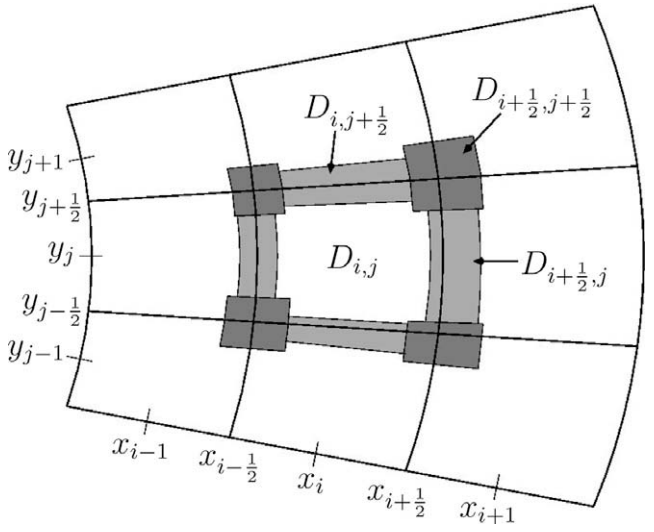

Fig. 1. Cellular structure for a non-Cartesian grid. Here we show nine cells, where only for the central one C_{ij} the regions that possibly contain discontinuities are highlighted by the grey areas. D_{ij}, at the same time, indicates the smooth central sub-region of cell C_{ij}.

t^{n+1} (denoted as $\bar{\omega}_{ij}^{n+1}$ for D_{ij}, $\bar{\omega}_{ij\pm\frac{1}{2}}^{n+1}$ for $D_{ij\pm\frac{1}{2}}$, $\bar{\omega}_{i\pm\frac{1}{2}j}^{n+1}$ for $D_{i\pm\frac{1}{2}j}$ and $\bar{\omega}_{i\pm\frac{1}{2}j\pm\frac{1}{2}}^{n+1}$ for $D_{i\pm\frac{1}{2}j\pm\frac{1}{2}}$). Secondly a piecewise polynomial reconstruction is obtained from these cell averages. This is written in a similar way as in Eq. (4):

$$\tilde{\omega}^{n+1}(x,y) := \sum_{ij}\left[\bar{\omega}_{ij}^{n+1}\tilde{\chi}_{ij} + \tilde{\omega}_{ij+\frac{1}{2}}^{n+1}\tilde{\chi}_{ij+\frac{1}{2}} + \tilde{\omega}_{i+\frac{1}{2}j}^{n+1}\tilde{\chi}_{i+\frac{1}{2}j} + \tilde{\omega}_{i+\frac{1}{2}j+\frac{1}{2}}^{n+1}\tilde{\chi}_{i+\frac{1}{2}j+\frac{1}{2}}\right] \tag{13}$$

Finally this reconstruction polynomial is projected back to the original grid (as was done for the first time in [13]) to yield cell averages again:

$$\bar{u}_{ij}^{n+1} = \frac{1}{|C_{ij}|}\int\int_{C_{ij}} \tilde{\omega}^{n+1}(\xi,\eta)h_1(\xi,\eta)h_2(\xi,\eta)d\xi\,d\eta \tag{14}$$

So far we have essentially discussed the derivation of the fully discrete scheme. As discussed in the introduction, we aim to derive a semi-discrete scheme. Taking, thus, into account that we will from now on be using $\Delta t \to 0$, we find for the area of the corner regions: $|D_{i\pm\frac{1}{2}j\pm\frac{1}{2}}| = \mathcal{O}(\Delta t^2)$ – in the following we will indicate areas by the use of vertical bars. Due to the fact that the area of the other regions which may contain discontinuities are of order Δt, the corner regions can be neglected in the semi-discrete version of the scheme. Keeping only terms up to the order of Δt, we thus find, for the regions possibly containing discontinuities defined by Eqs. (6) and (7):

$$D_{ij+\frac{1}{2}} \simeq [h_1(x_{i-\frac{1}{2}},y_{j+\frac{1}{2}})x_{i-\frac{1}{2}},\ h_1(x_{i+\frac{1}{2}},y_{j+\frac{1}{2}})x_{i+\frac{1}{2}}] \times [h_2(x_i,y_{j+\frac{1}{2}})y_{j+\frac{1}{2}} - b_{ij+\frac{1}{2}}^{-}\Delta t,\quad h_2(x_i,y_{j+\frac{1}{2}})y_{j+\frac{1}{2}} + b_{ij+\frac{1}{2}}^{+}\Delta t] \tag{15}$$

$$D_{i+\frac{1}{2}j} := [h_1(x_{i+\frac{1}{2}},y_j)x_{i+\frac{1}{2}} - a_{i+\frac{1}{2}j}^{-}\Delta t,\quad h_1(x_{i+\frac{1}{2}},y_j)x_{i+\frac{1}{2}} + a_{i+\frac{1}{2}j}^{+}\Delta t] \times [h_2(x_{i+\frac{1}{2}},y_{j-\frac{1}{2}})y_{j-\frac{1}{2}},\quad h_2(x_{i+\frac{1}{2}},y_{j+\frac{1}{2}})y_{j+\frac{1}{2}}] \tag{16}$$

For the intersection of the regions $D_{ij\pm\frac{1}{2}}$ and $D_{i\pm\frac{1}{2}j}$ with the cell C_{ij} we now introduce the notation:

$$S_{ij\pm\frac{1}{2}} = C_{ij}\cap D_{ij\pm\frac{1}{2}} \quad\text{and}\quad S_{i\pm\frac{1}{2}j} = C_{ij}\cap D_{i\pm\frac{1}{2}j} \tag{17}$$

Making use of this notation we find for the relation between $\tilde{\omega}^{n+1}$ and $\bar{\omega}^{n+1}$ in the different regions:

$$\int\int_{S_{ij\pm\frac{1}{2}}} \tilde{\omega}^{n+1}(\xi,\eta)h_1(\xi,\eta)h_2(\xi,\eta)d\xi d\eta = |S_{ij\pm\frac{1}{2}}|\bar{\omega}_{ij\pm\frac{1}{2}}^{n+1} + \mathcal{O}(\Delta t^2) \tag{18}$$

$$\int\int_{S_{i\pm\frac{1}{2}j}} \tilde{\omega}^{n+1}(\xi,\eta)h_1(\xi,\eta)h_2(\xi,\eta)d\xi d\eta = |S_{i\pm\frac{1}{2}j}|\bar{\omega}_{i\pm\frac{1}{2}j}^{n+1} + \mathcal{O}(\Delta t^2) \tag{19}$$

In the semi-discrete limit we will neglect any quantities of order $\mathcal{O}(\Delta t^2)$. For the smooth central region of the cell, however, we find without any approximation due to the conservation property of the reconstruction:

$$\int\int_{D_{ij}} \tilde{\omega}^{n+1}(\xi,\eta)h_1(\xi,\eta)h_2(\xi,\eta)d\xi d\eta = |D_{ij}|\bar{\omega}_{ij}^{n+1} \tag{20}$$

Thus, the only ingredients that are still missing for the computation of the scheme are the areas of the sub-regions and the local cell averages at the next time-step. In the semi-discrete limit the area of the non-smooth regions is approximately:

$$\left|S_{i\pm\frac{1}{2}j}\right| \simeq a_{i\pm\frac{1}{2}j}^{\mp}\Delta t\ h_2(x_{i\pm\frac{1}{2}},y_j)\Delta y \tag{21}$$

$$\left|S_{ij\pm\frac{1}{2}}\right| \simeq h_1(x_i,y_{j\pm\frac{1}{2}})\Delta x\ b_{ij\pm\frac{1}{2}}^{\mp}\Delta t \tag{22}$$

Together with Eqs. (18) and (19), we thus find:

$$\lim_{\Delta t\to 0}\frac{1}{\Delta t|C_{ij}|}\int\int_{S_{i\pm\frac{1}{2}j}} \tilde{\omega}_{i\pm\frac{1}{2}j}^{n+1}h_1(\xi,\eta)h_2(\xi,\eta)d\xi d\eta = \frac{h_2(x_{i\pm\frac{1}{2}},y_j)\Delta y}{|C_{ij}|}a_{i\pm\frac{1}{2}j}^{\mp}\lim_{\Delta t\to 0}\bar{\omega}_{i\pm\frac{1}{2}j}^{n+1} \tag{23}$$

$$\lim_{\Delta t\to 0}\frac{1}{\Delta t|C_{ij}|}\int\int_{S_{ij\pm\frac{1}{2}}} \tilde{\omega}_{ij\pm\frac{1}{2}}^{n+1}h_1(\xi,\eta)h_2(\xi,\eta)d\xi d\eta = \frac{h_1(x_i,y_{j\pm\frac{1}{2}})\Delta x}{|C_{ij}|}b_{ij\pm\frac{1}{2}}^{\mp}\lim_{\Delta t\to 0}\bar{\omega}_{ij\pm\frac{1}{2}}^{n+1} \tag{24}$$

The local cell averages are now obtained by integrating Eq. (2) over one time-step and over the corresponding sub-domains. The temporal and spatial integration yields for $\bar{\omega}_{i+\frac{1}{2}j}^{n+1}$ (the cell average for the region $D_{i+\frac{1}{2}j}$):

$$\left((a^+_{i+\frac{1}{2}j}+a^-_{i+\frac{1}{2}j})h_2(x_{i+\frac{1}{2}},y_j)\Delta y\right)\bar{\omega}^{n+1}_{i+\frac{1}{2}j} = \int_{y_{j-\frac{1}{2}}}^{y_{j+\frac{1}{2}}}\left(a^+_{i+\frac{1}{2}j}p^n_{i+1\,j}(x_{i+\frac{1}{2}},\eta)+a^-_{i+\frac{1}{2}j}p^n_{ij}(x_{i+\frac{1}{2}},\eta)\right.$$
$$\left.-\left(f_1(p^n_{i+1\,j}(x_{i+\frac{1}{2}},\eta))-f_1(p^n_{ij}(x_{i+\frac{1}{2}},\eta))\right)\right)h_2(x_{i+\frac{1}{2}},\eta)\,d\eta \tag{25}$$

and for the region $D_{ij+\frac{1}{2}}$:

$$\left((b^+_{ij+\frac{1}{2}}+b^-_{ij+\frac{1}{2}})h_1(x_i,y_{j+\frac{1}{2}})\Delta x\right)\bar{\omega}^{n+1}_{ij+\frac{1}{2}} = \int_{x_{i-\frac{1}{2}}}^{x_{i+\frac{1}{2}}}\left(b^+_{ij+\frac{1}{2}}p^n_{ij+1}(\xi,y_{j+\frac{1}{2}})+b^-_{ij+\frac{1}{2}}p^n_{ij}(\xi,y_{j+\frac{1}{2}})-\left(f_2(p^n_{ij+1}(\xi,y_{j+\frac{1}{2}}))\right.\right.$$
$$\left.\left.-f_2(p^n_{ij}(\xi,y_{j+\frac{1}{2}}))\right)\right)h_1(\xi,y_{j+\frac{1}{2}})\,d\xi \tag{26}$$

Even though we have the advantage that the central region does not contain any discontinuity, the corresponding expression is nonetheless the most complex to arrive at. Integration of the expression $\partial u/\partial t$ over the central part (in the semi-discrete limit, where this region is assumed to be of the same shape as the cell) and averaging over one time-step Δt yields:

$$\frac{1}{\Delta t}|D_{ij}|\left(\bar{\omega}^{n+1}_{ij}-\bar{\omega}^n_{ij}\right) \simeq \frac{1}{\Delta t}\left(|D_{ij}|\bar{\omega}^{n+1}_{ij}-\left(|C_{ij}|\bar{u}^n_{ij}-a^-_{i+\frac{1}{2}j}\Delta t\int_{y_{j-\frac{1}{2}}}^{y_{j+\frac{1}{2}}}p_{ij}(x_{i+\frac{1}{2}},\eta)h_2(x_{i+\frac{1}{2}},\eta)\,d\eta\right.\right.$$
$$-a^+_{i-\frac{1}{2}j}\Delta t\int_{y_{j-\frac{1}{2}}}^{y_{j+\frac{1}{2}}}p_{ij}(x_{i-\frac{1}{2}},\eta)h_2(x_{i-\frac{1}{2}},\eta)\,d\eta-b^-_{ij+\frac{1}{2}}\Delta t\int_{x_{i-\frac{1}{2}}}^{x_{i+\frac{1}{2}}}p_{ij}(\xi,y_{j+\frac{1}{2}})h_1(\xi,y_{i+\frac{1}{2}})\,d\xi$$
$$\left.\left.-b^+_{ij-\frac{1}{2}}\Delta t\int_{x_{i-\frac{1}{2}}}^{x_{i+\frac{1}{2}}}p_{ij}(\xi,y_{j-\frac{1}{2}})h_1(\xi,y_{i-\frac{1}{2}})\,d\xi\right)\right) \tag{27}$$

where $|D_{ij}|$ is the area of the central region of the cell D_{ij}. Integration of Eq. (2) over D_{ij} together with an averaging over one time-step then results in the following expression:

$$\begin{aligned}\frac{1}{\Delta t}|D_{ij}|\left(\bar{\omega}^{n+1}_{ij}-\bar{\omega}^n_{ij}\right) &= -\int_{D_{ij}}\frac{1}{h_1(\xi,\eta)h_2(\xi,\eta)}\left(\frac{\partial(h_2(\xi,\eta)f_1(u))}{\partial\xi}+\frac{\partial(h_1(\xi,\eta)f_2(u))}{\partial\eta}\right)h_1(\xi,\eta)h_2(\xi,\eta)\,d\xi\,d\eta\\ &\simeq -\int_{y_{j-\frac{1}{2}}}^{y_{j+\frac{1}{2}}}\left(h_2(x_{i+\frac{1}{2}},\eta)f_1(p_{ij}(x_{i+\frac{1}{2}},\eta))-h_2(x_{i-\frac{1}{2}},\eta)f_1(p_{ij}(x_{i-\frac{1}{2}},\eta))\right)d\eta\\ &\quad-\int_{x_{i-\frac{1}{2}}}^{x_{i+\frac{1}{2}}}\left(h_1(\xi,y_{j+\frac{1}{2}})f_2(p_{ij}(\xi,y_{j+\frac{1}{2}}))-h_1(\xi,y_{j-\frac{1}{2}})f_2(p_{ij}(\xi,y_{j-\frac{1}{2}}))\right)d\xi\end{aligned} \tag{28}$$

The combination of Eqs. (27) and (28), thus, leads to the following result for the central smooth area of the cell:

$$\begin{aligned}\lim_{\Delta t\to 0}\frac{1}{\Delta t}\left\{\frac{|D_{ij}|}{|C_{ij}|}\bar{\omega}^{n+1}_{ij}-\bar{u}^n_{ij}\right\} = &-\frac{a^-_{i+\frac{1}{2}j}}{|C_{ij}|}\int_{y_{j-\frac{1}{2}}}^{y_{j+\frac{1}{2}}}p_{ij}(x_{i+\frac{1}{2}},\eta)h_2(x_{i+\frac{1}{2}},\eta)\,d\eta-\frac{a^+_{i-\frac{1}{2}j}}{|C_{ij}|}\int_{y_{j-\frac{1}{2}}}^{y_{j+\frac{1}{2}}}p_{ij}(x_{i-\frac{1}{2}},\eta)h_2(x_{i-\frac{1}{2}},\eta)\,d\eta\\ &-\frac{b^-_{ij+\frac{1}{2}}}{|C_{ij}|}\int_{x_{i-\frac{1}{2}}}^{x_{i+\frac{1}{2}}}p_{ij}(\xi,y_{j+\frac{1}{2}})h_1(\xi,y_{j+\frac{1}{2}})\,d\xi-\frac{b^+_{ij-\frac{1}{2}}}{|C_{ij}|}\int_{x_{i-\frac{1}{2}}}^{x_{i+\frac{1}{2}}}p_{ij}(\xi,y_{j-\frac{1}{2}})h_1(\xi,y_{j-\frac{1}{2}})\,d\xi\\ &-\frac{1}{|C_{ij}|}\int_{y_{j-\frac{1}{2}}}^{y_{j+\frac{1}{2}}}\left(h_2(x_{i+\frac{1}{2}},\eta)f_1(p_{ij}(x_{i+\frac{1}{2}},\eta))-h_2(x_{i-\frac{1}{2}},\eta)f_1(p_{ij}(x_{i-\frac{1}{2}},\eta))\right)d\eta\\ &-\frac{1}{|C_{ij}|}\int_{x_{i-\frac{1}{2}}}^{x_{i+\frac{1}{2}}}\left(h_1(\xi,y_{j+\frac{1}{2}})f_2(p_{ij}(\xi,y_{j+\frac{1}{2}}))-h_1(\xi,y_{j-\frac{1}{2}})f_2(p_{ij}(\xi,y_{j-\frac{1}{2}}))\right)d\xi\end{aligned} \tag{29}$$

Finally we have to join all the above to find the evolution equation for the individual cell averages. Evaluating Eqs. (13) and (14) in the semi-discrete limit we find for the temporal evolution of the cell average $\bar{u}_{ij}$:

$$\begin{aligned}\frac{d}{dt}\bar{u}_{ij}(t) = &\lim_{\Delta t\to 0}\frac{1}{\Delta t\,|C_{ij}|}\left(\sum_{\pm}\int\int_{S_{ij\pm\frac{1}{2}}}\tilde{\omega}^{n+1}_{ij\pm\frac{1}{2}}h_1(\xi,\eta)h_2(\xi,\eta)d\xi d\eta+\int\int_{S_{i\pm\frac{1}{2}j}}\tilde{\omega}^{n+1}_{i\pm\frac{1}{2}j}h_1(\xi,\eta)h_2(\xi,\eta)d\xi d\eta\right)\\ &+\lim_{\Delta t\to 0}\frac{1}{\Delta t}\left(\frac{|D_{ij}|}{|C_{ij}|}\bar{\omega}^{n+1}_{ij}-\bar{u}^n_{ij}\right)\end{aligned} \tag{30}$$

Inserting all relevant quantities, yields – after a little algebra – the following result:

$$
\begin{aligned}
\frac{d}{dt}\bar{u}_{i,j}(t) \simeq & \frac{1}{a^{\pm}_{i+\frac{1}{2}}|C_{i,j}|}\int_{y_{j-\frac{1}{2}}}^{y_{j+\frac{1}{2}}}\left(a^{+}_{i+\frac{1}{2},j}a^{-}_{i+\frac{1}{2},j}(p^{n}_{i+1,j}(x_{i+\frac{1}{2}},\eta)-p^{n}_{i,j}(x_{i+\frac{1}{2}},\eta))\right)h_2(x_{i+\frac{1}{2}},\eta)\,d\eta \\
& -\frac{1}{a^{\pm}_{i-\frac{1}{2}}|C_{i,j}|}\int_{y_{j-\frac{1}{2}}}^{y_{j+\frac{1}{2}}}\left(a^{+}_{i-\frac{1}{2},j}a^{-}_{i-\frac{1}{2},j}(p^{n}_{i,j}(x_{i-\frac{1}{2}},\eta)-p^{n}_{i-1,j}(x_{i-\frac{1}{2}},\eta))\right)h_2(x_{i-\frac{1}{2}},\eta)\,d\eta \\
& +\frac{1}{b^{\pm}_{j+\frac{1}{2}}|C_{i,j}|}\int_{x_{i-\frac{1}{2}}}^{x_{i+\frac{1}{2}}}\left(b^{+}_{i,j+\frac{1}{2}}b^{-}_{i,j+\frac{1}{2}}(p^{n}_{i,j+1}(\xi,y_{j+\frac{1}{2}})+p^{n}_{i,j}(\xi,y_{j+\frac{1}{2}}))\right)h_1(\xi,y_{j+\frac{1}{2}})\,d\xi \\
& -\frac{1}{b^{\pm}_{j-\frac{1}{2}}|C_{i,j}|}\int_{x_{i-\frac{1}{2}}}^{x_{i+\frac{1}{2}}}\left(b^{+}_{i,j-\frac{1}{2}}b^{-}_{i,j-\frac{1}{2}}(p^{n}_{i,j}(\xi,y_{j-\frac{1}{2}})-p^{n}_{i,j-1}(\xi,y_{j-\frac{1}{2}}))\right)h_1(\xi,y_{j-\frac{1}{2}})\,d\xi \\
& -\frac{1}{a^{\pm}_{i+\frac{1}{2}}|C_{i,j}|}\int_{y_{j-\frac{1}{2}}}^{y_{j+\frac{1}{2}}}\left(a^{-}_{i+\frac{1}{2},j}f_1(p^{n}_{i+1,j}(x_{i+\frac{1}{2}},\eta))+a^{+}_{i+\frac{1}{2},j}f_1(p^{n}_{i,j}(x_{i+\frac{1}{2}},\eta))\right)h_2(x_{i+\frac{1}{2}},\eta)\,d\eta \\
& +\frac{1}{a^{\pm}_{i-\frac{1}{2}}|C_{i,j}|}\int_{y_{j-\frac{1}{2}}}^{y_{j+\frac{1}{2}}}\left(a^{-}_{i-\frac{1}{2},j}f_1(p^{n}_{i,j}(x_{i-\frac{1}{2}},\eta))+a^{+}_{i-\frac{1}{2},j}f_1(p^{n}_{i-1,j}(x_{i-\frac{1}{2}},\eta))\right)h_2(x_{i-\frac{1}{2}},\eta)\,d\eta \\
& -\frac{1}{b^{\pm}_{j+\frac{1}{2}}|C_{i,j}|}\int_{x_{i-\frac{1}{2}}}^{x_{i+\frac{1}{2}}}\left(b^{-}_{i,j+\frac{1}{2}}f_2(p^{n}_{i,j+1}(\xi,y_{j+\frac{1}{2}}))+b^{+}_{i,j+\frac{1}{2}}f_2(p^{n}_{i,j}(\xi,y_{j+\frac{1}{2}}))\right)h_1(\xi,y_{j+\frac{1}{2}})\,d\xi \\
& +\frac{1}{b^{\pm}_{j-\frac{1}{2}}|C_{i,j}|}\int_{x_{i-\frac{1}{2}}}^{x_{i+\frac{1}{2}}}\left(b^{-}_{i,j-\frac{1}{2}}f_2(p^{n}_{i,j}(\xi,y_{j-\frac{1}{2}}))+b^{+}_{i,j-\frac{1}{2}}f_2(p^{n}_{i,j-1}(\xi,y_{i-\frac{1}{2}}))\right)h_1(\xi,y_{i-\frac{1}{2}})\,d\xi
\end{aligned}
\tag{31}
$$

where we introduced the abbreviations:

$$a^{\pm}_{i+\frac{1}{2}} = a^{+}_{i+\frac{1}{2},j} + a^{-}_{i+\frac{1}{2},j} \tag{32}$$

$$b^{\pm}_{j+\frac{1}{2}} = b^{+}_{i,j+\frac{1}{2}} + b^{-}_{i,j+\frac{1}{2}} \tag{33}$$

Whenever the area of the cell can be approximated to a sufficiently high degree by:

$$|C_{i,j}| = h_1(x_i,y_j)\Delta x\; h_2(x_i,y_j)\Delta y \tag{34}$$

we can derive a convenient form of the evolution equation. By the introduction of the functions F and G this is:

$$\frac{d}{dt}\bar{u}_{i,j}(t) = -\frac{1}{h_1(x_i,y_j)h_2(x_i,y_j)}\left(\frac{F_{i+\frac{1}{2},j}(t)-F_{i-\frac{1}{2},j}(t)}{\Delta x}+\frac{G_{i,j+\frac{1}{2}}(t)-G_{i,j-\frac{1}{2}}(t)}{\Delta y}\right) \tag{35}$$

where F and G are given as:

$$
\begin{aligned}
F_{i-\frac{1}{2},j}(t) = & \frac{1}{a^{\pm}_{i-\frac{1}{2}}\Delta y}\int_{y_{j-\frac{1}{2}}}^{y_{j+\frac{1}{2}}}\left(a^{-}_{i-\frac{1}{2},j}f_1(p^{n}_{i,j}(x_{i-\frac{1}{2}},\eta))+a^{+}_{i-\frac{1}{2},j}f_1(p^{n}_{i-1,j}(x_{i-\frac{1}{2}},\eta))\right. \\
& \left.-a^{+}_{i-\frac{1}{2},j}a^{-}_{i-\frac{1}{2},j}(p^{n}_{i,j}(x_{i-\frac{1}{2}},\eta)-p^{n}_{i-1,j}(x_{i-\frac{1}{2}},\eta))\right)h_2(x_{i-\frac{1}{2}},\eta)\,d\eta
\end{aligned}
\tag{36}
$$

$$
\begin{aligned}
G_{i,j-\frac{1}{2}}(t) = & \frac{1}{b^{\pm}_{j-\frac{1}{2}}\Delta x}\int_{x_{i-\frac{1}{2}}}^{x_{i+\frac{1}{2}}}\left(b^{-}_{i,j-\frac{1}{2}}f_2(p^{n}_{i,j}(\xi,y_{j-\frac{1}{2}}))+b^{+}_{i,j-\frac{1}{2}}f_2(p^{n}_{i,j-1}(\xi,y_{j-\frac{1}{2}}))\right. \\
& \left.-b^{+}_{i,j-\frac{1}{2}}b^{-}_{i,j-\frac{1}{2}}(p^{n}_{i,j}(\xi,y_{j-\frac{1}{2}})-p^{n}_{i,j-1}(\xi,y_{j-\frac{1}{2}}))\right)h_1(\xi,y_{j-\frac{1}{2}})\,d\xi
\end{aligned}
\tag{37}
$$

We note:

- The CFL condition to satisfy the stability criterion for the above explicit scheme is given the constraint that the regions containing the Riemann fans must not intersect. This is ensured by:

$$\Delta t < \min\left(\frac{h_1(x_{i\pm\frac{1}{2}},y_j)\Delta x}{2}\frac{1}{\max(a^{\pm}_{i\pm\frac{1}{2}}+v^{0}_{x})},\frac{h_2(x_i,y_{j\pm\frac{1}{2}})\Delta y}{2}\frac{1}{\max(b^{\pm}_{j\pm\frac{1}{2}}+v^{0}_{y})}\right) \tag{38}$$

- Be aware that the functions F and G are no direct approximations to the *physical* flux functions. This is due to the presence of the scale factors in the corresponding equations, because these are in general dimensional quantities. To obtain approximations of the physical flux functions, the order of the scheme has to be specified, thus determining how the integrals in Eqs. (36) and (37) are to be evaluated. Thereafter the scale factors can be included into the evolution equation itself.
- The scheme is also valid for a Cartesian mesh. In this case all geometrical scale factors are unity. Thus Eq. (35) is transformed into the same form as Eq. (3.30) in [16]. The same is true for the corresponding flux functions given in Eqs.

(36) and (37), which are reduced to the corresponding Eqs. (3.34) and (3.35) in [16] when the integrals are evaluated using the second order midpoint rule.

Eqs. (35)–(37) represent a general form for the multi-dimensional central scheme for arbitrary grid-geometries. The important point is that the geometric factors are introduced self-consistently. Thus there is no discussion as to where they have to appear. Apart from that, the scheme was derived in a most general way. To derive an actual workable scheme one has to choose the desired order of the scheme and the grid geometry. The order is fixed by the choice of a corresponding reconstruction polynomial, which then also determines the form of the integrals over the cell boundaries. To illustrate this behaviour we will derive a scheme for plane polar coordinates in the next section.

3. Special form of the numerical scheme

Many problems in physics have inherent symmetries, which suggest the use of a plane polar grid geometry to solve these problems. Therefore, we will illustrate the derivation of a working scheme from the general results given in Section 2 using the example of plane polar coordinates. For these we have the following coordinates and geometrical factors:

$$(x,y) = (r,\phi), \quad (h_1,h_2) = (1,r) \tag{39}$$

Obviously the geometrical factors only depend on the first coordinate (and, thus, only on the index i). Apart from that, Eq. (34) is the exact form for the area of a cell in plane polar coordinates. Therefore, we can use Eq. (35) to derive the scheme in plane polar coordinates, yielding:

$$\frac{d}{dt}\bar{u}_{ij}(t) = -\frac{F_{i+\frac{1}{2}j}(t) - F_{i-\frac{1}{2}j}(t)}{\Delta r} - \frac{G_{ij+\frac{1}{2}}(t) - G_{ij-\frac{1}{2}}(t)}{r_i \Delta\phi} \tag{40}$$

together with the order independent numerical flux functions evaluated from Eqs. (36) and (37):

$$F_{i-\frac{1}{2}j}(t) = \frac{r_{i-\frac{1}{2}}}{a^{\pm}_{i-\frac{1}{2}} r_i \Delta\phi} \int_{\phi_{j-\frac{1}{2}}}^{\phi_{j+\frac{1}{2}}} \left(a^{-}_{i-\frac{1}{2}j} f_1(p^n_{ij}(r_{i-\frac{1}{2}},\eta)) + a^{+}_{i-\frac{1}{2}j} f_1(p^n_{i-1j}(r_{i-\frac{1}{2}},\eta)) - a^{+}_{i-\frac{1}{2}j} a^{-}_{i-\frac{1}{2}j}(p^n_{ij}(r_{i-\frac{1}{2}},\eta) - p^n_{i-1j}(r_{i-\frac{1}{2}},\eta)) \right) d\eta \tag{41}$$

$$G_{ij-\frac{1}{2}}(t) = \frac{1}{b^{\pm}_{j-\frac{1}{2}} \Delta r} \int_{r_{i-\frac{1}{2}}}^{r_{i+\frac{1}{2}}} \left(b^{-}_{ij-\frac{1}{2}} f_2(p^n_{ij}(\xi,\phi_{j-\frac{1}{2}})) + b^{+}_{ij-\frac{1}{2}} f_2(p^n_{ij-1}(\xi,\phi_{j-\frac{1}{2}})) - b^{+}_{ij-\frac{1}{2}} b^{-}_{ij-\frac{1}{2}}(p^n_{ij}(\xi,\phi_{j-\frac{1}{2}}) - p^n_{ij-1}(\xi,\phi_{j-\frac{1}{2}})) \right) d\xi \tag{42}$$

To be able to evaluate the above integrals we chose the resulting scheme to be of second order. Thus, the midpoint rule is sufficient for the computation of the integrals. In this case we find for the numerical fluxes:

$$F_{i-\frac{1}{2}j}(t) = \frac{r_{i-\frac{1}{2}}}{a^{\pm}_{i-\frac{1}{2}} r_i} \left(a^{-}_{i-\frac{1}{2}j} f_1(p^n_{ij}(r_{i-\frac{1}{2}},\phi_j)) + a^{+}_{i-\frac{1}{2}j} f_1(p^n_{i-1j}(r_{i-\frac{1}{2}},\phi_j)) - a^{+}_{i-\frac{1}{2}j} a^{-}_{i-\frac{1}{2}j}(p^n_{ij}(r_{i-\frac{1}{2}},\phi_j) - p^n_{i-1j}(r_{i-\frac{1}{2}},\phi_j)) \right) \tag{43}$$

$$G_{ij-\frac{1}{2}}(t) = \frac{1}{b^{\pm}_{j-\frac{1}{2}}} \left(b^{-}_{ij-\frac{1}{2}} f_2(p^n_{ij}(r_i,\phi_{j-\frac{1}{2}})) + b^{+}_{ij-\frac{1}{2}} f_2(p^n_{ij-1}(r_i,\phi_{j-\frac{1}{2}})) - b^{+}_{ij-\frac{1}{2}} b^{-}_{ij-\frac{1}{2}}(p^n_{ij}(r_i,\phi_{j-\frac{1}{2}}) - p^n_{ij-1}(r_i,\phi_{j-\frac{1}{2}})) \right) \tag{44}$$

For the reconstruction polynomial we use the following prescription in order to guarantee the non-oscillatory behaviour.

$$p^n_{ij}(r_{i-\frac{1}{2}},\phi_j) = \bar{u}_{ij} - \frac{1}{2}\Delta r\ u^r_{ij}\ p^n_{i-1j}(r_{i-\frac{1}{2}},\phi_j) = \bar{u}_{i-1j} + \frac{1}{2}\Delta r\ u^r_{i-1j} \text{ with}$$
$$u^r_{ij} = \text{minmod}\left(\theta \frac{u^n_{ij} - u^n_{i-1j}}{\Delta r}, \frac{u^n_{i+1j} - u^n_{i-1j}}{2\Delta r}, \theta \frac{u^n_{i+1j} - u^n_{ij}}{\Delta r} \right) \tag{45}$$

with corresponding definitions for the ϕ direction. Here a larger $\theta \in [1,2]$ corresponds to a less dissipative but still *non-oscillatory* limiter. This limiter was already discussed in Ref. [34]. It is explicitly defined by:

$$\text{minmod}(a,b,c) := \begin{cases} \text{sign}(a)\min(|a|,|b|,|c|) & \text{if} \quad \text{sign}(a) = \text{sign}(b) = \text{sign}(c) \\ 0 & \text{else} \end{cases} \tag{46}$$

For this limiter it can be shown that the reconstruction is not only non-oscillatory but also total-variation diminishing (TVD) (see, e.g., [16]). This reconstruction guarantees oscillations to be suppressed at steep gradients as will be shown when the different tests are discussed.

Finally, for the time integration we use a third order TVD Runge–Kutta scheme as is given in Refs. [30,31], which completes our algorithm. We will use this scheme to demonstrate the feasibility of this approach by several test-cases in the next paragraph. Since one of these numerical experiments is actually using cylindrical coordinates, we will, however, first introduce the corresponding scheme.

For (fully three-dimensional) cylindrical coordinates the scheme can be derived in two equivalent ways: either the scheme is derived from the general prescription given in Appendix A, or the above scheme for plane polar coordinates is just extended in the z-direction. Here we just state the result. Using the following coordinates and geometrical factors:

$$(x,y,z) = (r,\phi,z), \quad (h_1,h_2,h_3) = (1,r,1) \tag{47}$$

we find for the scheme in cylindrical coordinates:

$$\frac{d}{dt}\bar{u}_{i,j,k}(t) = -\frac{F_{i+\frac{1}{2},j,k}(t) - F_{i-\frac{1}{2},j,k}(t)}{\Delta r} - \frac{G_{i,j+\frac{1}{2},k}(t) - G_{i,j-\frac{1}{2},k}(t)}{r_i \Delta\phi} - \frac{H_{i,j,k+\frac{1}{2}}(t) - H_{i,j,k-\frac{1}{2}}(t)}{\Delta z} \tag{48}$$

with the numerical fluxes:

$$F_{i-\frac{1}{2},j,k}(t) = \frac{r_{i-\frac{1}{2},k}}{a^{\pm}_{i-\frac{1}{2}} r_i}\Big(a^{-}_{i-\frac{1}{2},j,k} f_1(p^n_{i,j,k}(r_{i-\frac{1}{2}}, \phi_j, z_k)) + a^{+}_{i-\frac{1}{2},j,k} f_1(p^n_{i-1,j,k}(r_{i-\frac{1}{2}}, \phi_j, z_k)) \\ - a^{+}_{i-\frac{1}{2},j,k} a^{-}_{i-\frac{1}{2},j,k}(p^n_{i,j,k}(r_{i-\frac{1}{2}}, \phi_j, z_k) - p^n_{i-1,j,k}(r_{i-\frac{1}{2}}, \phi_j, z_k))\Big) \tag{49}$$

$$G_{i,j-\frac{1}{2},k}(t) = \frac{1}{b^{\pm}_{j-\frac{1}{2}}}\Big(b^{-}_{i,j-\frac{1}{2},k} f_2(p^n_{i,j,k}(r_i, \phi_{j-\frac{1}{2}}, z_k)) + b^{+}_{i,j-\frac{1}{2},k} f_2(p^n_{i,j-1,k}(r_i, \phi_{j-\frac{1}{2}}, z_k)) \\ - b^{+}_{i,j-\frac{1}{2},k} b^{-}_{i,j-\frac{1}{2},k}(p^n_{i,j,k}(r_i, \phi_{j-\frac{1}{2}}, z_k) - p^n_{i,j-1,k}(r_i, \phi_{j-\frac{1}{2},z_k}))\Big) \tag{50}$$

$$H_{i,j,k-\frac{1}{2}}(t) = \frac{1}{c^{\pm}_{k-\frac{1}{2}}}\Big(c^{-}_{i,j,k-\frac{1}{2}} f_3(p^n_{i,j,k}(r_i, \phi_j, z_{k-\frac{1}{2}})) + c^{+}_{i,j,k-\frac{1}{2}} f_3(p^n_{i,j,k-1}(r_i, \phi_j, z_{k-\frac{1}{2}})) \\ - c^{+}_{i,j,k-\frac{1}{2}} c^{-}_{i,j,k-\frac{1}{2}}(p^n_{i,j,k}(r_i, \phi_j, z_{k-\frac{1}{2}}) - p^n_{i,j,k-1}(r_i, \phi_j, z_{k-\frac{1}{2}}))\Big) \tag{51}$$

The time integration and the reconstruction are done in an analogous way to the scheme in plane polar coordinates. This concludes the derivation of the schemes applied in the numerical experiments to be discussed in the subsequent section.

4. Numerical tests

To demonstrate the validity and study the accuracy of our numerical scheme we performed several numerical experiments based on the so-called Euler equations. These are a system of hyperbolic equations describing compressible hydrodynamical flows. They are given as:

$$\frac{\partial \rho}{\partial t} = -\nabla \cdot (\rho \mathbf{u}) \tag{52}$$

$$\frac{\partial (\rho \mathbf{u})}{\partial t} = -\nabla \cdot (\rho \mathbf{u}\mathbf{u} + p1) + \mathbf{S} \tag{53}$$

$$\frac{\partial e}{\partial t} = -\nabla \cdot ((e + p)\mathbf{u}) \tag{54}$$

where ρ is the mass density, $\mathbf{u}$ is the flow velocity, p is the pressure and 1 is the unit matrix. The pressure is connected to the total energy density via:

$$e = \frac{p}{\gamma - 1} + \frac{1}{2}\rho \mathbf{u}^2 \tag{55}$$

Due to the tensorial character of the fluxes for the momentum equation, we have to include additional source terms to Eq. (53). In particular, we find for our cylindrical coordinate system that we have to include source terms for the r and ϕ momentum equations. Specifically, these are the inertial terms

$$S_r = \frac{\rho \mathrm{v}_\phi^2 + p}{r} \quad \text{and} \quad S_\phi = \frac{-\rho \mathrm{v}_r \mathrm{v}_\phi}{r} \tag{56}$$

In the subsequent paragraphs we describe several numerical experiments using the Euler equations, which will serve as tests for different aspects of the numerical scheme. For the following numerical experiments please be aware that all of the quantities will be given in non-dimensional form.

4.1. The order of the scheme

To verify the order of the scheme we used two simple tests in plane polar coordinates. For the first we advected a small amplitude sine-disturbance in the azimuthal direction for one full revolution. Setting the radial velocity to zero this test can be shown to correspond to a Cartesian advection test and indeed yields the same results. In particular the form of the disturbance is conserved by the scheme and it approaches second order for high spatial resolutions.

For the radial direction we adopted a simple advection test introduced by [33]. This test is initialised by a constant density and a velocity field proportional to the radial distance from the origin of a cylindrical coordinate system ($v_r = v_0 r$). Keeping the velocity constant with time we find for the temporal evolution of the density:

$$\rho(t) = \rho_0 e^{-2v_0 t} \tag{57}$$

As suggested in [33] we integrate the decaying density up to time $t = 6$, where we have chosen $v_0 = 1$. Thus, we have a change of the density of more than five orders of magnitude.

To investigate the order of the scheme we compared the numerical results for several spatial resolutions (the radial domain extending from $r = 0.4$ to $r = 2.5$ was partitioned into 16-256 cells) to the above analytical solution. We show the dependence of the corresponding normalised error on the number of grid-cells in Fig. 2. Obviously the error decreases quadratically with increasing spatial resolution. Thus, the scheme is still of second order despite the presence of the geometrical scale factors.

4.2. The Sedov explosion in plane polar coordinates

A numerical experiment which is particularly suited for the test of a code on a plane polar grid is the Sedov explosion problem (see [29]). In this test a localised enhancement of the thermal energy is injected into an otherwise homogeneous and static background medium. This energy enhancement evolves into a radial blast wave in a self-similar fashion. The problem is similar to the shock tube test problem used for one-dimensional tests on Cartesian grids (see, e.g., [32]) in that there exists a semi-analytical solution. Thus, it is possible to test whether the code yields the correct shock-strength, -location and -speed. This is a condition which has to be fulfilled by every conservative code. Therefore, it is a good indication to find out whether the geometrical factors are correctly implemented.

The Sedov problem is initialised via a localised pressure enhancement at the origin of the form:

$$e_{init} = \frac{\epsilon}{V_{Init}} = \frac{3\epsilon}{(v+2)\pi\delta r^{v+1}} \tag{58}$$

Here, γ is the adiabatic exponent, which is chosen to be $\gamma = 1.4$ for all Sedov tests in this work. ϵ is the energy to be added to the simulation domain and V_{Init} is the volume of the region, into which the energy is added. On the right hand side we state the expression in an explicit form for an arbitrary number of spatial dimensions, where r denotes the distance from the origin of the coordinate system. Here $v = 1$ corresponds to the two-dimensional (planar) Sedov explosion and $v = 2$ to the genuinely three-dimensional case.

We solved the Sedov problem for cylindrical coordinates on a radial grid from 0 to 0.5, which was decomposed into 200 equidistant cells in the radial direction. For the azimuthal direction and the vertical direction we only used a single cell in this test. Hence it is a one-dimensional test of the plane polar coordinate system. The background thermal energy was chosen as $e_{th} = 10^{-5}$ and the blast was initialised with an energy of $\epsilon = 1$, which was distributed over the three inner grid-cells. The time-step for the simulations was adapted such that the CFL number never exceeded 0.4.

The results of the corresponding simulations are compared to the semi-analytical solution in Fig. 3 for the normalised time $t = 0.1$. Obviously the numerical solution for the density and the velocity perfectly fits to the analytical results. This leads to the conclusion that the pressure part of the source term S_r and also the geometrical factors are indeed given correctly in our formulation. The correctness of the other directions will be tested by further simulations, which take more general geometries into account.

4.3. Sedov explosion in cylindrical coordinates

Naturally the above test can be made for any grid geometry. After having shown that the radial part of the Euler equations is working correctly, we now have to take care of the other components. For the first of these tests we again make use of the Sedov problem. This time, however, we investigate the Sedov problem in three spatial dimensions. We are using

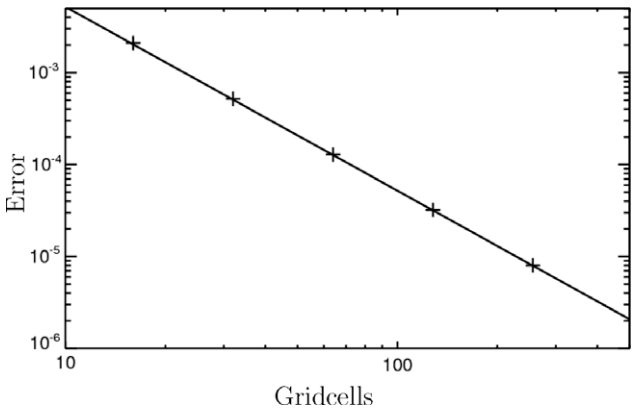

Fig. 2. Dependence of the relative numerical error of the density on spatial resolution. The solid line corresponds to a quadratic decrease of the numerical error.

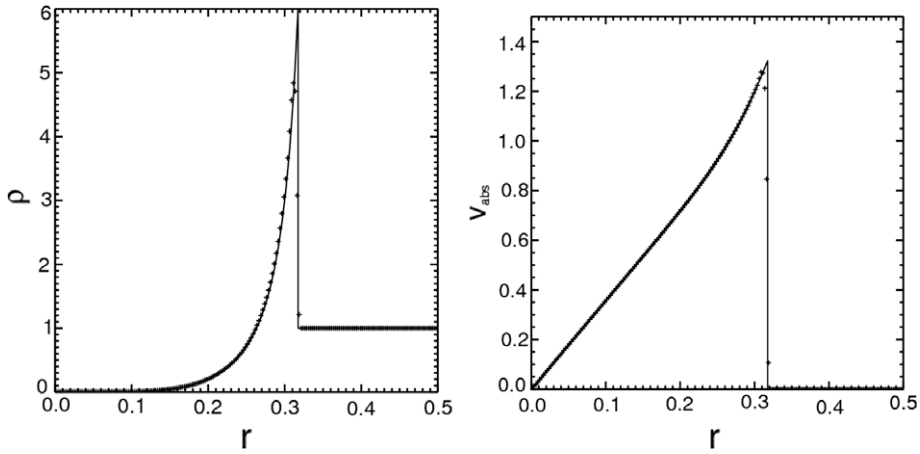

Fig. 3. Results for the Sedov explosion problem in plane polar coordinates at time $t = 0.1$. On the left the density is shown as a function of the radius. On the right the velocity is shown in a similar fashion. In both figures the analytical solution is superimposed as the solid line.

cylindrical coordinates, thus yielding a test-case for which the evolution of the shock is not aligned to either the r or the z-axis.

The simulations were done with a resolution of 200 grid-points in the radial and the z-direction. For the azimuthal direction we again took only one grid-point into account (the correctness of this direction will be confirmed by the next test-problem). Results of these simulations are depicted in Figs. 4 and 5. In the former of these we show contours for the thermal energy and the density. Obviously the spherical nature of the problem is nicely captured by the code. Now we have to check whether the speed and the strength of the radial shock wave are also computed correctly.

To show this we computed a scatter plot for the different quantities, i.e., we plot the value of the individual quantities over the distance to the origin of the blast wave for each individual cell in the computational domain. The corresponding results for the density are given in Fig. 5. Also in this numerical test the data nicely follow the analytical solution. As in the preceding test the shock again can be seen to be at the correct position with the correct strength.

Thus, we can conclude that on one hand, the geometrical terms are correct for the radial and the z-direction, and on the other hand, the code is still sufficiently conservative to yield the correct shock solutions, even though the inclusion of the additional source terms might disturb this feature of the code. Now we finally come to a numerical experiment, which can be used to demonstrate the correctness of the code also for the azimuthal direction.

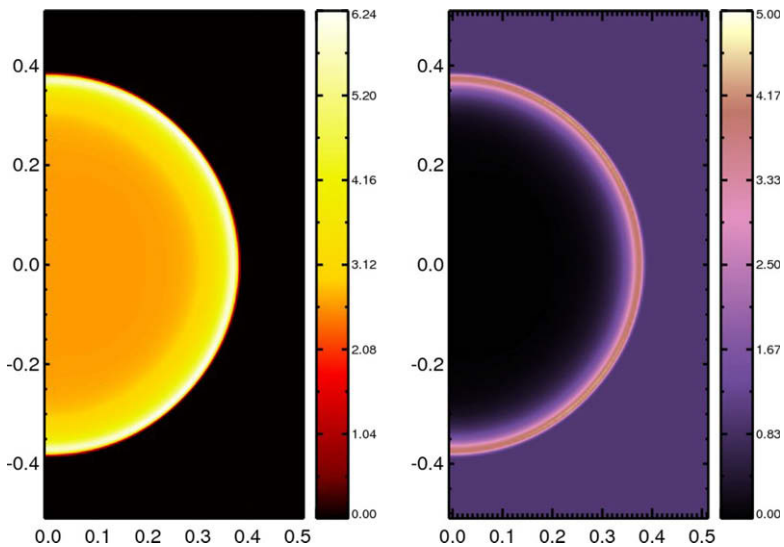

Fig. 4. Results for the Sedov explosion problem in cylindrical coordinates at time $t = 0.08$. On the left we show the thermal energy distribution and on the right the density. These quantities are shown for a given ϕ, where the radius goes to the right and z to the top.

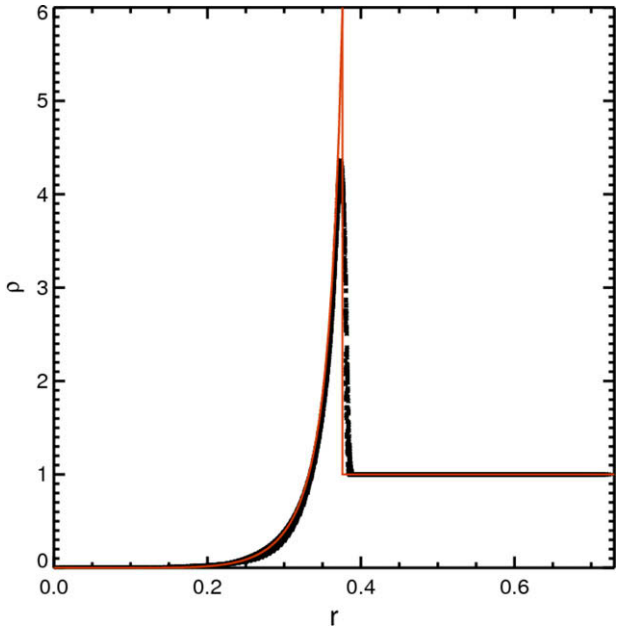

Fig. 5. Scatter plot for the density for the Sedov problem. The individual data-points indicate the density at all grid-points in the numerical domain. The density values are plotted as a function of the distance from the origin of the explosion. The data are given for the time $t = 0.08$.

4.4. A general problem

The most general problem to be investigated as a test here is the classical Shock tube problem, which was already mentioned above. This test can be used as a strictly one-dimensional problem in Cartesian geometry. Here, however, we will apply this test to plane polar coordinates, which are clearly not adapted to the problem.

This numerical experiment is initialised by the introduction of a contact discontinuity at $x + y = 0.5$, with different density- and pressure-values on both sides of the discontinuity. In particular we choose for the initial conditions:

$$[\rho(x), p(x)] = \begin{cases} [10, 100] & \text{if } x + y < 0.5 \\ [1, 1] & \text{if } x + y \geqslant 0.5 \end{cases} \tag{59}$$

where the adiabatic exponent is again chosen to be $\gamma = 1.4$. This is a modified version of the original problem, which yields even stronger shocks (see, e.g., [7]). Like in the preceding tests there exists a semi-analytical solution for this problem. Thus, we can investigate the results in a similar manner as done above. We used the analytical solution to prescribe the boundary conditions at ϕ_{min} and ϕ_{max}. At r_{min} and r_{max} we used extrapolating boundaries. We decided to use the analytical solution at the ϕ-boundaries in order to avoid any spurious oscillations, which might be introduced by an extrapolation procedure near the resulting shock wave. The simulation was run with a spatial resolution of 200 grid-points in the radial and the azimuthal directions. The time-step was changed adaptively so that the CFL number never exceeded 0.2.

Due to the fact that the geometry of the numerical grid does not fit to the problem this setup constitutes a test for all the geometrical factors and also all the momentum source terms included in the scheme. Due to the presence of the resulting shock wave we can also test the conservation properties of the code.

In Fig. 6 the resulting thermal energy contours are shown. It is obvious that the shock front is very straight even though the coordinates are not adapted to the problem. Also there are no apparent spurious oscillations. As in the previous tests, however, we have to quantify the results in order to make sure the shocks are correct with regard to their strength and position. To this end we show a scatter plot for the resulting density in the same figure. The individual data-points are given as a function of their perpendicular distance to some reference line parallel to the initial contact discontinuity. In this plot the initial discontinuity was at $x = 0.5$. The comparison to the analytical solution (shown in red) demonstrates the excellent agreement of the numerical results to the analytical predictions. As in the previous tests the shocks are again at the proper position with the correct strength. Moreover, there are no spurious oscillations.

The same test was run with a similar configuration for a 3D system in spherical coordinates. The results were similar to the ones shown for plane polar coordinates. Again, the shock was in the correct position with the correct strength. To keep this presentation concise, however, we refrain from discussing this numerical experiment.

After this test, we can conclude that the numerical scheme has been derived and implemented correctly. There are no problems originating from the geometrical factors or the source terms in the numerical scheme. Obviously the resulting

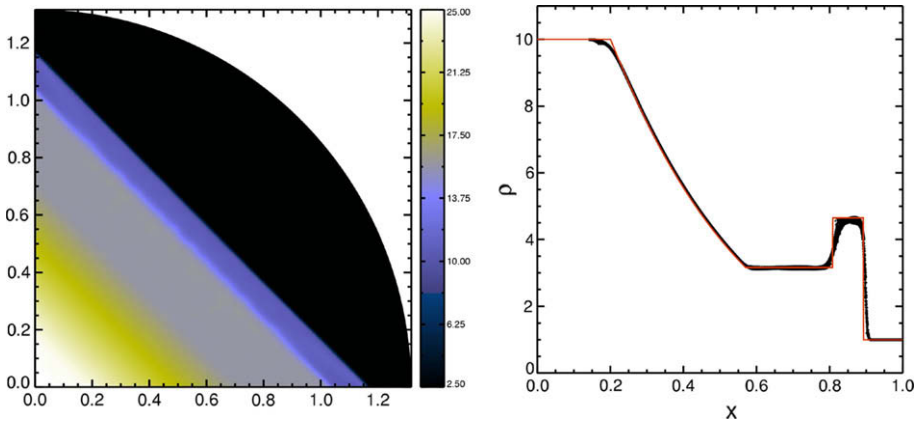

Fig. 6. (Left) colour contours for the results of the shock tube problem in plane polar coordinates. Shown is the thermal energy. (Right) scatter plot for the density of the shock tube problem in plane polar coordinates. The data are compared to the analytical solution (shown in red). In both plots we see on the left the undisturbed medium followed by a rarefaction wave. The sharp increase of the density is a contact discontinuity, which is finally followed by a shock. Both figures are given for time $t = 0.08$. (For interpretation of the references to color in this figure legend, the reader is referred to the web version of this article.)

scheme is still sufficiently conservative so that shocks in the numerical experiments are reproduced correctly regardless of their orientation with respect to the grid.

5. Conclusion

In this paper we have constructed of a numerical scheme for the integration of hyperbolic partial differential equations on general rectangular grids. The scheme has been constructed in a most general way leaving the choice of the order of the scheme through a choice of the reconstruction polynomial to the user. After the general derivation we demonstrated the construction of an actual numerical scheme from the general equations. For this we used the example of plane polar and cylindrical coordinates.

For this scheme we showed several numerical experiments, for all of which we found excellent agreement of the numerical results with corresponding analytical solutions. Thus, we were able to demonstrate the correct derivation and implementation of the scheme.

The method introduced in this paper can easily be extended to more than two dimensions. The resulting scheme is a straightforward extension of Eqs. (35)–(37). It can be shown, that the intuitive extension directly yields the correct results. We will, however, refrain from doing so in this paper due to the huge amount of algebra. Instead we will just give the corresponding results in Appendix A.

In realistic physical systems the conservation of quantities such as mass, energy and angular momentum plays a very important role. The appearance of source terms in the momentum equations on the right hand side may formally destroy these conservation properties. We point out that in the case of the important angular momentum a minor reformulation of the equation will explicitly bring it into conservative form again.

Acknowledgements

This work was partially financed by the Deutsche Forschungsgemeinschaft (DFG) through the project KL 650/6 and benefitted form the Finnish-German cooperation funded via DAAD 313-SF-PPP Finnland. Additional financial support from the Vilho, Yrjö, and Kalle Väisälä foundation is acknowledged. W. Kley acknowledges support by the DFG through Forschergruppe FOR 759. Computational resources were provided in the Project hbo25 by the Forschungszentrum Jülich.

Appendix A. The three-dimensional scheme

The general scheme for three dimensions can be derived in an analogous way to the two-dimensional scheme. Here we will only state the results skipping the lengthy algebra. For the temporal evolution of the cell average $\bar{u}(x, y, z)$ we find:

$$\frac{d}{dt}\bar{u}_{i,j,k}(t) = -\frac{F_{i+\frac{1}{2},j,k}(t) - F_{i-\frac{1}{2},j,k}(t)}{|C_{i,j,k}|} - \frac{G_{i,j+\frac{1}{2},k}(t) - G_{i,j-\frac{1}{2},k}(t)}{|C_{i,j,k}|} - \frac{H_{i,j,k+\frac{1}{2}}(t) - H_{i,j,k-\frac{1}{2}}(t)}{|C_{i,j,k}|} \tag{A.1}$$

where the numerical fluxes F, G and H are given as:

$$F_{i-\frac{1}{2}j,k}(t) = \frac{1}{a^{\pm}_{i-\frac{1}{2}}} \int_{y_{j-\frac{1}{2}}}^{y_{j+\frac{1}{2}}} \int_{z_{k-\frac{1}{2}}}^{z_{k+\frac{1}{2}}} d\eta\, d\sigma h_2(x_{i-\frac{1}{2}},\eta,\sigma) h_3(x_{i-\frac{1}{2}},\eta,\sigma) \times \Big(a^{-}_{i-\frac{1}{2}j,k} f_1(p^n_{i,j,k}(x_{i-\frac{1}{2}},\eta,\sigma)) + a^{+}_{i-\frac{1}{2}j,k} f_1(p^n_{i-1,j,k}(x_{i-\frac{1}{2}},\eta,\sigma)) \quad \text{(A.2)}$$
$$- a^{+}_{i-\frac{1}{2}j,k} a^{-}_{i-\frac{1}{2}j,k} \Big(p^n_{i,j,k}(x_{i-\frac{1}{2}},\eta,\sigma) - p^n_{i-1,j,k}(x_{i-\frac{1}{2}},\eta,\sigma) \Big) \Big)$$

$$G_{ij-\frac{1}{2},k}(t) = \frac{1}{b^{\pm}_{j-\frac{1}{2}}} \int_{x_{i-\frac{1}{2}}}^{x_{i+\frac{1}{2}}} \int_{z_{k-\frac{1}{2}}}^{z_{k+\frac{1}{2}}} d\xi d\sigma h_1(\xi,y_{j-\frac{1}{2}},\sigma) h_3(\xi,y_{j-\frac{1}{2}},\sigma) \times \Big(b^{-}_{ij-\frac{1}{2},k} f_2(p^n_{i,j,k}(\xi,y_{j-\frac{1}{2}},\sigma)) + b^{+}_{ij-\frac{1}{2},k} f_2(p^n_{ij-1,k}(\xi,y_{j-\frac{1}{2}},\sigma)) \quad \text{(A.3)}$$
$$- b^{+}_{ij-\frac{1}{2},k} b^{-}_{ij-\frac{1}{2},k} \Big(p^n_{i,j,k}(\xi,y_{j-\frac{1}{2}},\sigma) - p^n_{ij-1,k}(\xi,y_{j-\frac{1}{2}},\sigma) \Big) \Big)$$

$$H_{i,j,k-\frac{1}{2}}(t) = \frac{1}{c^{\pm}_{k-\frac{1}{2}}} \int_{x_{i-\frac{1}{2}}}^{x_{i+\frac{1}{2}}} \int_{y_{j-\frac{1}{2}}}^{y_{j+\frac{1}{2}}} d\xi d\eta h_1(\xi,\eta,z_{k-\frac{1}{2}}) h_2(\xi,\eta,z_{k-\frac{1}{2}}) \times \Big(c^{-}_{i,j,k-\frac{1}{2}} f_3(p^n_{i,j,k}(\xi,\eta,z_{k-\frac{1}{2}})) + c^{+}_{i,j,k-\frac{1}{2}} f_3(p^n_{i,j,k-1}(\xi,\eta,z_{i-\frac{1}{2}})) \quad \text{(A.4)}$$
$$- c^{+}_{i,j,k-\frac{1}{2}} c^{-}_{i,j,k-\frac{1}{2}} \Big(p^n_{i,j,k}(\xi,\eta,z_{k-\frac{1}{2}}) - p^n_{i,j,k-1}(\xi,\eta,z_{k-\frac{1}{2}}) \Big) \Big)$$

Here we indicated the volume of the cell as $| C_{i,j,k} |$.

References

[1] P. Arminjon, D. Stanescu, M.-C. Viallon, A two-dimensional finite volume extension of the Lax–Friedrichs and Nessyahu–Tadmor schemes for compressible flow, in: H. Hafez, K. Oshima (Eds.), Proceedings of the Sixth International Symposium on Computational Fluid Dynamics, Lake Tahoe, CA, 1995, pp. 7–14.
[2] P. Arminjon, D. Stanescu, M.-C. Viallon, A. Madrane, A finite volume extension of the Lax–Friedrichs and Nessyahu–Tadmor schemes for conservation laws on unstructured grids, Int. J. Comput. Fluid Dyn. 9 (1997) 1–22.
[3] P. Arminjon, M.-C. Viallon, Généralisation du schéma de Nessyahu–Tadmor pour une équation hyperbolique à deux dimensions d'espace, C.R. Avad. Sci. Paris Sér. I Math. 320 (1995) 85–88.
[4] P. Arminjon, M.-C. Viallon, Convergence of a finite volume extension of the Nessyahu–Tadmor scheme on unstructured grids for a two-dimensional linear hyperbolic equation, SIAM J. Numer. Anal. 36 (3) (1999) 738–771.
[5] J. Balbás, E. Tadmor, C.-C. Wu, Non-oscillatory central schemes for one- and two-dimensional MHD equations: I, J. Comput. Phys. 201 (2004) 261–285.
[6] F. Bianco, G. Puppo, G. Russo, High order central schemes for hyperbolic systems of conservation laws, SIAM J. Sci. Comput. 21 (1999) 294–322.
[7] A.C. Calder, B. Fryxell, T. Plewa, R. Rosner, L.J. Dursi, V.G. Weirs, T. Dupont, H.F. Robey, J.O. Kane, B.A. Remington, R.P. Drake, G. Dimonte, M. Zingale, F.X. Timmes, K. Olson, P. Ricker, P. MacNeice, H.M. Tufo, On Validating an Astrophysical Simulation Code, ApJS 143 (2002) 201–229.
[8] R. Courant, K. Friedrichs, H. Lewy, Über die partiellen Differenzengleichungen der mathematischen Physik, Math. Ann. 100 (1928) 32–74.
[9] K.O. Friedrichs, P.D. Lax, Systems of conservation equations with a convex extension, Proc. Nat. Acad. Sci. 68 (1971) 1686–1688.
[10] S.K. Godunov, Finite difference method for numerical computation of discontinuous solution of the equations of fluid dynamics, Mater. Sb. 47 (1959) 271.
[11] A. Harten, High resolution schemes for hyperbolic conservation laws, J. Comput. Phys. 49 (1983) 357–393.
[12] A. Harten, Uniformly high order accurate essentially non-oscillatory schemes, III, J. Comput. Phys. 71 (1987) 231–303.
[13] G.-S. Jiang, D. Levy, C.-T. Lin, S. Osher, E. Tadmor, High-resolution nonoscillatory central schemes with nonstaggered grids for hyperbolic conservation laws, SIAM J. Numer. Anal. 35 (1998) 2147–2168.
[14] G.-S. Jiang, C.-W. Shu, Efficient implementation of weighted ENO schemes, J. Comput. Phys. 126 (1996) 202–228.
[15] A. Kurganov, D. Levy, A third-order semidiscrete central scheme for conservation laws and convection–diffusion equations, SIAM J. Sci. Comput. 22 (2000) 1461–1488.
[16] A. Kurganov, S. Noelle, G. Petrova, Semidiscrete central-upwind schemes for hyperbolic conservation laws and Hamilton–Jacobi equations, SIAM J. Sci. Comput. 23 (3) (2001) 707–740.
[17] A. Kurganov, G. Petrova, A third-order semi-discrete genuinely multidimensional central scheme for hyperbolic conservation laws and related problems, Numer. Math. 88 (2001) 683–729.
[18] A. Kurganov, G. Petrova, Central-upwind schemes on triangular grids for hyperbolic systems of conservation laws, Num. Meth. PDEs 21 (2005) 536–552.
[19] A. Kurganov, E. Tadmor, New high resolution central schemes for nonlinear conservation laws and convection–diffusion equations, JCP 160 (2000) 241–282.
[20] Leveque, J. Randall, Finite Volume Methods for Hyperbolic Problems, Cambridge University Press, 2002.
[21] D. Levy, G. Puppo, G. Russo, Central WENO schemes for hyperbolic systems of conservation laws, Math. Model. Numer. Anal. 33 (1999) 547–571.
[22] D. Levy, G. Puppo, G. Russo, A third order central WENO scheme for 2D conservation laws, Appl. Numer. Math. 33 (2000) 407–414.
[23] D. Levy, G. Puppo, G. Russo, Compact central WENO schemes for multidimensional conservation laws, SIAM J. Sci. Comput. 22 (2000) 656–672.
[24] X.D. Liu, S. Osher, T. Chan, Weighted essentially non-oscillatory schemes, J. Comput. Phys. 115 (1994) 200–212.
[25] X.D. Liu, E. Tadmor, Third order nonoscillatory central scheme for hyperbolic conservation on laws, Numer. Math. 79 (1998) 397–425.
[26] H. Nessyahu, E. Tadmor, Non-oscillatory central differencing for hyperbolic conservation laws, J. Comput. Phys. 87 (1990) 408–463.
[27] S. Osher, E. Tadmor, On the convergence of difference approximations to scalar conservation laws, Math. Comput. 50 (181) (1988) 19–51.
[28] S. Osher, E. Tadmor, On the convergence of difference approximations to scalar conservation laws, SIAM J. Sci. Comput. 5 (1990) 127–149.
[29] L.I. Sedov, Similarity and Dimensional Methods in Mechanics, Academic Press, New York, 1959.
[30] C.-W. Shu, Total-variation-diminishing time discretizations, SIAM J. Sci. Stat. Comput. 9 (6) (1988) 1073–1084.
[31] C.-W. Shu, S. Osher, Efficient implementation of essentially non-oscillatory shock-capturing schemes, II, J. Comput. Phys. 83 (1989) 32–78.
[32] G. Sod, A survey of several finite difference methods for systems of nonlinear hyperbolic conservation laws, J. Comput. Phys. 27 (1978) 1–31.
[33] J.M. Stone, M.L. Norman, ZEUS-2D: a radiation magnetohydrodynamics code for astrophysical flows in two space dimensions. I. The hydrodynamic algorithm and tests, ApJS 80 (1992) 753–790.
[34] B. van Leer, Towards the ultimate conservative difference scheme, V. A second order sequel to Godunov's method, J. Comput. Phys. 32 (1979) 101–136.